

Signatures of Cosmic Reionization on the 21cm 2- and 3-point Correlation Function I: Quadratic Bias Modeling

Kai Hoffmann¹, Yi Mao¹, Houjun Mo^{1,2}, Benjamin D. Wandelt^{3,4,5}

¹*Department of Physics and Tsinghua Center for Astrophysics, Tsinghua University, Beijing 100084, China*

²*Department of Astronomy, University of Massachusetts, Amherst MA 01003-9305, USA*

³*Institut d'Astrophysique de Paris (IAP), Institut Lagrange de Paris (ILP), UMR 7095, CNRS, UPMC Universit Paris 6, Sorbonne Universits, 98bis boulevard Arago, F-75014 Paris, France*

⁴*Department of Physics and Astronomy, University of Illinois at Urbana-Champaign, 1002 W Green St, Urbana, IL 61801, USA*

⁵*Center for Computational Astrophysics, Flatiron Institute, 162 5th Avenue, New York, NY 10010, USA*

Accepted XXX. Received YYY; in original form ZZZ

ABSTRACT

Constraints on reionization models from future 21cm observations will rely on the statistical characterization of the spatial fluctuations in the observed 21cm brightness temperature. Three-point correlation functions (3PCF) of this 21cm signal probe information about the shape of ionized regions and can therefore improve constraints on reionization model from the power spectrum which is not sensitive to such shape information. We study the 21cm two-point correlation functions (2PCF) and 3PCF in configuration space, using semi-numerical simulations. These measurements are compared to leading order predictions from the local quadratic bias model, which is commonly used for modeling the galaxy 3PCF. Fits of the bias model predictions to the 2PCF and 3PCF measurements show an $\simeq 20\%$ accuracy for scales above the typical size of ionized regions ($\simeq 30$ Mpc) and at early times for global neutral fractions of $\langle x_{\text{HI}} \rangle \gtrsim 0.7$, while deviations between the predictions and measurements increase strongly for smaller scales and later reionization stages.

In the regime in which the bias model performs well, the 2PCF and 3PCF fits of the linear bias parameter agree at the 10% level. The relation between fluctuations in the matter density and the 21cm signal, as predicted by the bias model, is consistent with simulations for large smoothing scales. Our results suggest that measurements of the 3PCF in upcoming radio observations can constrain astrophysical processes driving the reionization. Combining the 21cm 2PCF and 3PCF can further break the degeneracy between the linear growth function of matter fluctuations and the reionization bias parameters, and hence constrain cosmological models during the epoch of reionization.

Key words: cosmology: Reionization - methods: statistical - numerical - analytical

1 INTRODUCTION

Upcoming radio observations, such as those of the SKA-LOW¹ or HERA² projects, will ring in a new era of cosmology, allowing us to observe the distribution of neutral hydrogen (HI) in the early universe at unprecedented scales and distances. These observations will provide novel insights into how the first light emitting objects ionized their surrounding gas. This so-called Epoch of Reionization (EoR) leads to the almost completely ionized universe, which we see today and can be characterized by the large scale HI

distribution at different times. This distribution is traced by the light, emitted during the HI hyper-fine transition at the wavelength of 21cm. Today we can observe this light as radio signals, since its was redshifted during its journey through the expanding universe (Field 1958). The 21cm signal is expected to show large-scale spatial fluctuations, which reflect the inhomogeneous matter distribution in the universe. Current EoR models suggest that these fluctuations are overlaid by patches without any 21cm emission, which are filled with ionized gas around the first luminous objects (e.g. Sokasian et al. 2004). The upcoming 21cm observations contain therefore not only information about how matter density fluctuations grow with time due to gravity, but also about how the first luminous objects form and transfer en-

¹ www.skatelescope.org

² www.reionization.org

ergy to the intergalactic medium (e.g. Furlanetto et al. 2006; Pritchard & Loeb 2012). Extracting this information from observations requires a statistical description of the 21cm fluctuations. Correlation functions proved to be useful tools for this purpose. Studies on the two-point correlation function of the 21cm EoR signal, or the power spectrum, as its Fourier space counterpart, revealed its high sensitivity to the underlying EoR model (e.g. Pober et al. 2014). This opens up the possibility to use this statistics to constrain EoR models with future observations (e.g. Liu & Parsons 2016). However, a restriction to one or two-point statistics prevents access to information on the morphology of the ionized regions, which is one of the most prominent features in simulated maps of the 21cm signal. Only recently studies probe this additional information using the three-point correlation in Fourier space, i.e. the bispectrum (Shimabukuro et al. 2016). The results revealed a strong dependence of the bispectrum on the scale, as well as on the shape of the triangles from which this statistics is measured (Majumdar et al. 2017). This additional information from the bispectrum can strongly improve power spectrum constraints on EoR model parameters (Shimabukuro et al. 2017).

Deriving such constraints from observations requires predictions for the 21cm statistics, which can be obtained from either theoretical modeling, or from simulations. In the latter case a large number of simulations is needed for a sufficiently dense sampling of the high dimensional EoR parameter space. In addition, these simulations need to cover a wide dynamical range to accurately predict the formation of ionizing sources at scales of $\lesssim 1$ Mpc and simultaneously the transfer of their radiation to the intergalactic medium on scales of up to $\simeq 20$ Mpc. Furthermore, the simulation volume needs to be sufficiently large to allow for precise measurements of the chosen statistics. These requirements can be met currently only with approximate simulation methods or emulation techniques (e.g. Mesinger et al. 2011; Schmit & Pritchard 2017).

Alternatively to simulations, predictions for the 21cm correlations function can be obtained from theoretical models. Such models have been presented for the 21cm power spectrum by Furlanetto et al. (2004); Lidz et al. (2007), while the only model for the 21cm bispectrum (to our knowledge) is restricted to the simplistic case of randomly distributed ionized spheres, which show similarities with simulation results only on small scales (Bharadwaj & Pandey 2005; Majumdar et al. 2017).

The goal of this work is to further develop the theoretical understanding of the two-point and in particular the three-point correlation function of the 21cm brightness temperature (hereafter referred to as 2PCF and 3PCF respectively), based on measurements in simulations. Our investigation of the 21cm 3PCF is performed for the first time in configuration space, which may simplify the physical interpretation of our results. To interpret our measurements, we employ the quadratic bias model, which has been developed to model the 3PCF of large-scale halo and galaxy distributions (Fry & Gaztanaga 1993). In the context of 21cm statistics, this model assumes that the matter density in a given volume of the universe determines the 21cm brightness temperature in that same volume, while the form of this deterministic relation is characterized by a set of free

parameters. This bias model allows for a perturbative approximation of the 21cm 2PCF and 3PCF, which depend at leading order on the two free bias parameters b_1 and b_2 .

We test the bias modeling using a set of 200 simulations, which we generate with the semi-numerical code 21cmFAST (Mesinger et al. 2011). The simulations differ only in their random initial conditions and cover a total volume of $\simeq (4.5 \text{ Gpc})^3$, providing robust measurements of the 21cm 2PCF and 3PCF, as well as estimates for the error covariance.

This paper is structured in the following way. We start by presenting our simulation in Section 2. The bias model is introduced in Section 3 where we also verify how well its prediction for the 2PCF and the 3PCF agree with the measurements in the simulations. As a second step in the model validation we compare the bias parameters from 2PCF and 3PCF fits in Section 4. Using these bias parameters, we further test in that section how the relation between the matter and 21 brightness temperature, predicted by the bias model compares to direct measurements of this relation in simulations. Our results are summarized in Section 5, where we also draw conclusions from our analysis.

2 SIMULATION

Our analysis is based on simulated three dimensional maps of the matter density and the 21cm brightness temperature, produced by the semi-numerical code 21cmFAST (Mesinger et al. 2011). The 21cm brightness temperature is given by

$$\delta T \simeq x_{\text{HI}}(1 + \delta_m) \left(\frac{T_s - T_{\text{CMB}}}{T_s} \right) \times \text{const} \quad (1)$$

with

$$\text{const} = \left(\frac{0.15}{\Omega_M} \right)^{1/2} \left(\frac{\Omega_b h^2}{0.023} \right) \text{mK}$$

(e.g. Furlanetto 2006). The term $x_{\text{HI}}(1 + \delta_m)$ corresponds to the HI density, while x_{HI} is the HI fraction of the total hydrogen density. We thereby assume a linear relation between the hydrogen and the full matter densities. The normalized spatial fluctuation of the total matter density, ρ_m , around the universal mean $\langle \rho_m \rangle$ is given by

$$\delta_m \equiv (\rho_m - \langle \rho_m \rangle) / \langle \rho_m \rangle. \quad (2)$$

The fluctuations $\delta_{\delta T}$, with which we will work later as well are defined analogously. We assume for simplicity that δT is dominated by the spin temperature T_s , while contributions from the Cosmic Microwave Background are negligible, i.e. $T_s \gg T_{\text{CMB}}$. This approximation is reasonable at the redshifts studied in this work (e.g. Zaldarriaga et al. 2004; Pritchard & Furlanetto 2007; Mesinger et al. 2011), but needs to be reconsidered for a more detailed analysis.

For further simplification we neglect modifications of the 21cm signal due to redshift space distortions. This may be an appropriate assumption for an analysis of projected 21cm signals in redshift bins. However, studies on three dimensional 21cm power spectra found notable contributions on large scales, in particular for early times with high neutral fractions, which should be included in a detailed modeling (McQuinn et al. 2006; Mesinger & Furlanetto 2007). For

a fast production of 21cm maps 21FAST first derives the evolved matter density distribution using the Zel'dovich approximation, starting from an initial Gaussian random field. We thereby set the matter and baryon density at redshift $z = 0$ to $\Omega_M = 0.308$ and $\Omega_b = 0.0226/h^2$ respectively, with $h = 0.678$. The spectral index is set to $n_s = 0.968$.

The ionized regions and the resulting 21cm signal are computed in a second step, using a semi-numerical approach, which is based on the excursion set formalism (Zaldarriaga et al. 2004). For this simulation step we set the minimum virial temperature for ionizing sources to $T_{vir} = 5 \cdot 10^4$ K and the ionizing efficiency parameter to $\zeta_{ion} = 60$. The calculations are performed on grids of cubical cells with side lengths of 0.5 and 1.5 Mpc for matter and HI respectively. The simulations are run in cubical volumes of $(768 \text{ Mpc})^3$ with periodic boundaries. To estimate the error covariance of our measured statistics we generate a set of 200 independent realizations with different random initial conditions, which cover a total volume of $(\sim 4.5 \text{ Gpc})^3$.

In Fig. 1 we show the simulated distributions of the dark matter density fluctuations and the 21cm brightness temperature of one realization at different redshifts in a 1.5 Mpc slice of a $(200 \text{ Mpc})^3$ sub volume. One can see how ionized regions start to form around the largest dark matter overdensities at high redshifts and connect with each other, as they grow with decreasing redshift. This growth progresses relatively fast compared to the growth of the large-scale matter density fluctuations. The redshift evolution of the global volume weighted neutral fraction $\langle x_{HI} \rangle$ is shown in Fig. 2. In Fig. 3 we show the probability distribution of the sizes of ionized regions, averaged over different random realizations. The sizes are measured by 21cmFAST by choosing random positions in the simulation and measuring the distance to the next phase transition in a randomly chosen direction. They reach scales 1 – 100 Mpc, while the maxima of the distributions lie at around 1 and 10 Mpc for $\langle x_{HI} \rangle = 0.99$ and 0.7 respectively.

3 BIASED CORRELATION FUNCTIONS

We quantify the clustering of the matter density and 21cm brightness temperature with 2- and 3-point correlation functions (hereafter referred to as 2PCF and 3PCF respectively). The convenience of these statistics arises from the fact, that they are well defined as well as theoretically extensively studied, since they are a common tools in galaxy clustering analysis (e.g. Bernardeau et al. 2002). A result of these studies, which is particularly useful for our analysis, is that the correlation functions of tracers of the total matter field, can be related to the matter correlation via so-called bias models as explained in the following.

3.1 Quadratic bias model

In the context of 21cm observations, a local bias model corresponds to a function F , which describes a deterministic relation between the fluctuations δ_m and $\delta_{\delta T}$, defined by equation (2), in a region of size R around a given position \mathbf{r} , i.e. $\delta_{\delta T}(\mathbf{r}) = F[\delta_m(\mathbf{r})]$. The term local refers to the model assumption, that $\delta_{\delta T}$ is solely determined by δ_m in the same

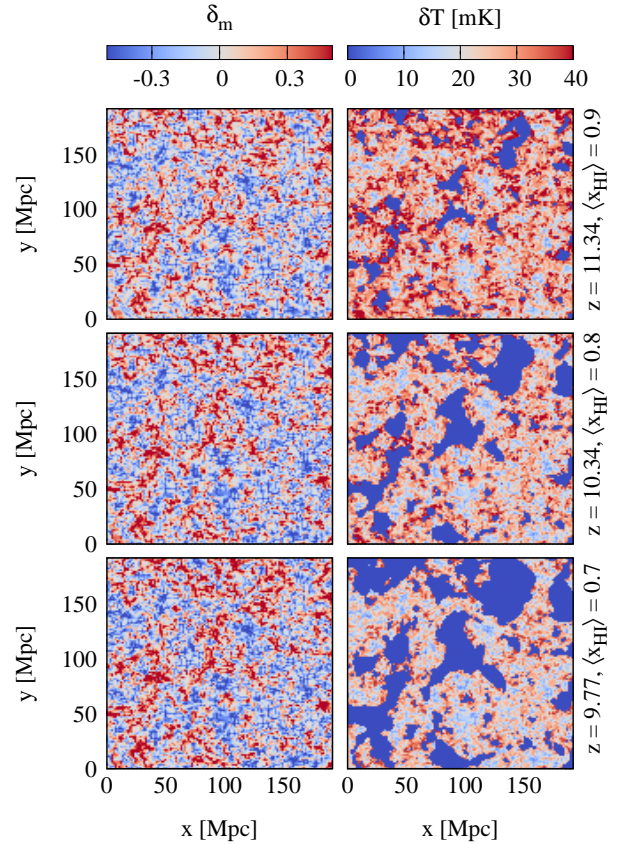


Figure 1. Simulated dark matter density fluctuations and 21cm brightness temperature (left and right panels respectively) in a 1.5 Mpc slice of a $(200 \text{ Mpc})^3$ sub volume in one realization. Results are shown for three redshift with different fractions of neutral hydrogen $\langle x_{HI} \rangle$. Patches of ionized gas with zero 21cm emission form around the highest matter overdensities at early times (top panels) and expand with decreasing redshift (central and bottom panels.)

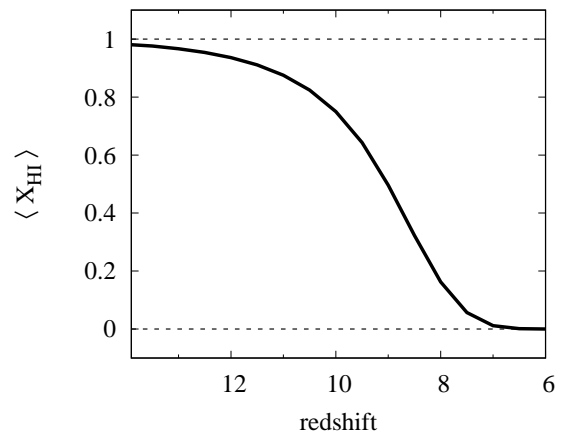


Figure 2. Global neutral hydrogen fraction, weighted by volume, versus redshift. Results are shown for one realization, while the variation for different realization is at the percent level.

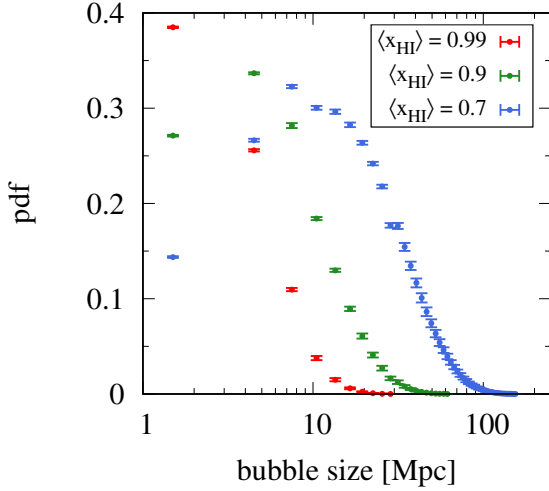


Figure 3. Size distribution of ionized regions (referred to as bubbles), measured by 21cmFAST at three different redshifts studied in this work with different mean neutral fractions. Dots show mean measurements from different random realizations with error bars denoting the corresponding standard deviations

region. This assumption can be violated, for instance by ionizing radiation, originating from over densities outside of the region (e.g. Furlanetto et al. 2004), or the tidal field, induced by the surrounding matter distribution, which affects the formation of halos in that region, which host the ionizing sources (Chan et al. 2012; Baldauf et al. 2012). However, for sufficiently large smoothing scales and early stages of the reionization, the deterministic approximation might be adequate, as we will see later in this analysis.

The form of the bias function is unknown at this point, but we can approximate it with a Taylor series around $\delta_m = 0$, assuming that $\delta_{\delta T}$ varies only weakly with δ_m , i.e. $\delta_{\delta T} \simeq \sum_{n=0}^N (b_n/n!) \delta_m^n$, where b_n are the bias parameters. The bias model provides a way to relate the 2PCF and 3PCF of δT to the corresponding statistics of the underlying matter field. For establishing these relations for up to third-order statistics, we need to expand the bias function to second order (see Fry & Gaztanaga 1993), i.e.

$$\delta_{\delta T} \simeq b_0 + b_1 \delta_m + b_2 \delta_m^2. \quad (3)$$

Requiring $\langle \delta_{\delta T} \rangle = 0$ sets the constrain $b_0 = -b_2 \sigma_m^2$, while the matter variance is given by $\sigma_m^2 = \langle \delta_m^2 \rangle$. Here $\langle \dots \rangle$ denotes the spatial average of the universe. The remaining free parameters b_1 and b_2 are referred to as linear and quadratic bias parameters respectively.

3.2 2-point correlation functions (2PCF)

The 2PCF can be defined via the product of fluctuations at two different positions

$$\xi(r) \equiv \langle \delta_1 \delta_2 \rangle(r), \quad (4)$$

where δ_i are the fluctuations of either the matter density or δT at the position \mathbf{r}_i and $\langle \dots \rangle$ denotes the average over all possible orientations and translations of the $\delta_i \delta_j$ pairs, separated by the distance $r \equiv |\mathbf{r}_2 - \mathbf{r}_1|$. In the following we will denote the 2PCFs of the matter and 21cm brightness

temperature fluctuations as ξ_m and $\xi_{\delta T}$ and refer to the latter as 21cm 2PCF. Due to the average over all orientations, the 2PCF is only sensitive to the scale dependence of the clustering, but not to the shape of large-scale structures. As a second order statistics, it is also not sensitive to a skewness in the probability distribution of δ_i . This additional information can be accessed via the 3PCF, which will be introduced in Section 3.3. Our 2PCF measurements are performed on a grid of cubical cells with 6 Mpc side lengths. We therefore define the fluctuations δ_m and $\delta_{\delta T}$ in each cell and then search for pairs of cells to obtain the average from equation (4).

The mean 2PCF measurements from our 200 realizations are shown versus the scale r for various redshifts with different global neutral fractions $\langle x_{\text{HI}} \rangle$ in Fig. 4. The matter 2PCF shows the expected strong scale dependence, while the amplitude increases only weakly with decreasing redshifts (decreasing neutral fractions), due to the slow growth of matter fluctuations at early times. We have verified that our matter 2PCF measurement are in good agreement with theory predictions based on the initial power spectrum of the simulation for $r \lesssim 90$ Mpc. Tests with simulations in boxes with twice the side length (i.e. 1536 Mpc) revealed that our 2PCF measurements at scales above $r \gtrsim 90$ Mpc are significantly affected by the limited box size, which causes an artificial cut-off of large wave length modes (see Appendix A). We therefore exclude 2PCF measurements from scales above 90 Mpc from our analysis.

A much stronger redshift evolution occurs for the 2PCF of δT as the amplitude first decreases, between $\langle x_{\text{HI}} \rangle = 0.99$ and 0.90, before it increases strongly for lower redshifts with lower neutral fractions. The shapes of the 21cm 2PCFs are very similar to those of the matter 2PCF, while being shifted by a roughly constant factor. This latter behaviour can be expected from the bias model, since inserting equation (3) into the 2PCF definition from equation (4) delivers at leading order in δ_m

$$\xi_{\delta T} \simeq b_1^2 \xi_m. \quad (5)$$

Note that alternatively to this prediction, a physically better motivated relation between the $\xi_{\delta T}$ and ξ_m can be derived by inserting the definition of δT from equation (1) into the 2PCF definition. However, current models based on this approach involve various approximations, which limit their accuracy (e.g. Furlanetto et al. 2004; Lidz et al. 2007; Raste & Sethi 2017). Furthermore, this approach becomes more challenging, for statistics beyond second-order statistics, such as the 3PCF.

We fit the linear bias model for $\xi_{\delta T}$ from equation (5) to our measurements between 40 – 90 Mpc via a χ^2 minimization, as detailed in Appendix B. Note we can thereby only infer the absolute value of the linear bias parameters, since it enters appears as b_1^2 in equation (5). However, we will see later on that b_1 can take positive as well as negative values. The fits are shown as solid lines in the top panel of Fig. 4. They deviate from the measurements by 10 – 20% with the fitting range for $\langle x_{\text{HI}} \rangle \gtrsim 0.6$ (bottom panel of Fig. 4). The strong deviations at large scales for lower global neutral fractions indicate a breakdown of the local bias model at late times of the reionization. Deviations from the fits also increase at small scales below 30 Mpc, which correspond roughly to the typical sizes of ionized regions, shown in Fig.

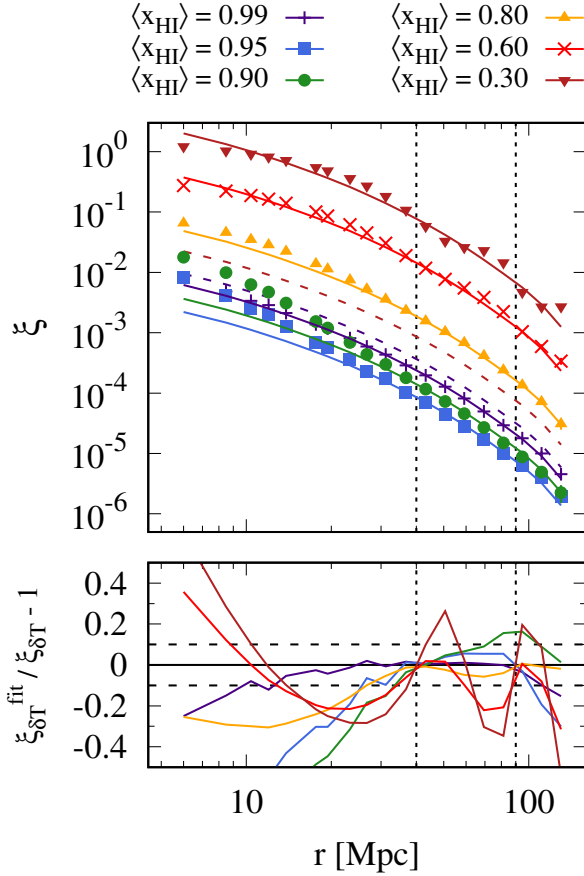


Figure 4. *Top:* 2PCF of the dark matter field and δT at different global neutral fractions $\langle x_{\text{HI}} \rangle$ (dashed lines and dots respectively) versus the scale r . Results are shown as means over measurements in 200 random realizations of the simulation. The 1σ measurement errors are smaller than the symbol size. Solid lines show fits to the 21cm 2PCF measurements, based on the bias model prediction from equation (5). The fitting range (40 – 90 Mpc) is enclosed by vertical black short-dashed lines. *Bottom:* Relative deviations between fits and measurements. Horizontal black dashed lines show 10% deviations.

3. Deviations at large scales may partly be explained by the aforementioned box size effect.

3.3 3-point correlation functions (3PCF)

The 3PCF is defined analogously to the 2PCF as

$$\zeta(r_1, r_2, \alpha) \equiv \langle \delta_1 \delta_2 \delta_3 \rangle(r_1, r_2, r_3). \quad (6)$$

The positions of the fluctuations δ_i form a triangle, with three legs of the sizes r_{1-3} . As for the 2PCF, $\langle \dots \rangle$ denotes the average over all possible rotations and translations. We will denote the 3PCFs of the matter and 21cm brightness temperature fluctuations as ζ_m and $\zeta_{\delta T}$ respectively, and refer to the latter as 21cm 3PCF. Our 3PCF measurements are performed on the same type of grid on which we compute the 2PCF. To search for triplets of grid cells, we employ the algorithm suggested by Barriga & Gaztañaga (2002). This algorithm delivers measurements for triangles with two fixed legs (r_1, r_2) and different leg sizes r_3 . The cell size is set to 6 or 12 Mpc for small and large triangles respectively,

to optimize the computation time. We have verified for the triangle configurations $(r_1, r_2) = (72, 36)$ and $(48, 48)$ Mpc, that the effect of the cell size on the 3PCF measurements is within the 1σ errors, except for triangles for which r_3 is comparable to the cell size. In general it is expected, that the 3PCF depends on the smoothing scale (i.e. the cell size), while we expect the effect on our analysis to be small, since we will focus on large scales. Tests on the scale dependence of our results are presented later on in this paper.

Examples of our 3PCF measurements for two configurations with fixed legs $(r_1, r_2) = (36, 36)$ and $(54, 30)$ Mpc at redshift $z = 9.77$ ($\langle x_{\text{HI}} \rangle = 0.7$) are shown in Fig. 5 for 18 opening angles $\alpha \equiv \cos(\hat{r}_1 \cdot \hat{r}_2)$ between 0 and 180 degree versus the corresponding size of the third triangle leg r_3 . The matter 3PCF, displayed in the top panels, has positive values for collapsed and relaxed triangles (small and large r_3 respectively), while being negative for half open triangles. This typical shape is a signature of the filamentary structure of the cosmic web (e.g. Bernardeau et al. 2002), and hence provides additional information about the dark matter distribution to which one- or two-point statistics are not sensitive to.

The corresponding measurements for the 21cm 3PCF, shown in the bottom panels of Fig. 5, are negative for all triangles, while their overall shape appears to be similar to the matter 3PCF. This result indicates, that there is a physical relation between the 3PCF of matter and δT . This relation can be approximated analogously to case of the 2PCF by a perturbative expansion of the 21cm 3PCF, using the bias model from equation (3). Inserting this model into the 3PCF definition from equation (6) delivers at leading order

$$\zeta_{\delta T} \simeq b_1^3 \zeta_m + b_1^2 b_2 \zeta_m^H \quad (7)$$

(Fry & Gaztanaga 1993). The hierarchical three-point correlation, $\zeta^H \equiv \xi_{12}\xi_{13} + 2 \text{ perm.}$ is shown as dashed-dotted lines in the top panels of Fig. 5.

We derive b_1 and b_2 from the 3PCF by fitting equation (7) to our measurements. The fits, shown as red lines in the bottom panels of Fig. 5, are obtained from a χ^2 minimization. The χ^2 values are computed via a Singular Value Decomposition (SVD) of the covariance matrix (the latter is shown in Fig. B2), as suggested by Gaztañaga & Scoccimarro (2005) to reduce the impact of noise in the covariance on our fits (see Appendix B for details). We fit the model only to measurements from triangles, for which all legs are in the range 30–90 Mpc. This selection is motivated by our 2PCF results, which showed, that the bias model prediction breaks down at smaller scales, while measurements at large scales may be affected by the limited box size (see Section 3.2).

Our fits are in reasonable agreement with the measurements within the fitting range, which shows that the quadratic bias model can explain the dominating part of the 21cm 3PCF signal at large scales. However, the fits deviate strongly from our measurements at small scales, below the minimum fitting scale. This indicates a break down of the bias model, according to which a given set of fitted bias parameters should describe the 21cm 3PCF at all scales.

The redshift evolution of the 21cm 3PCF is shown for triangles with $(r_1, r_2) = (48, 48)$ Mpc versus r_3 in Fig. 6. On large scales the 21cm 3PCF has negative values and a positive slope at early time ($\langle x_{\text{HI}} \rangle \gtrsim 0.5$). At later times the

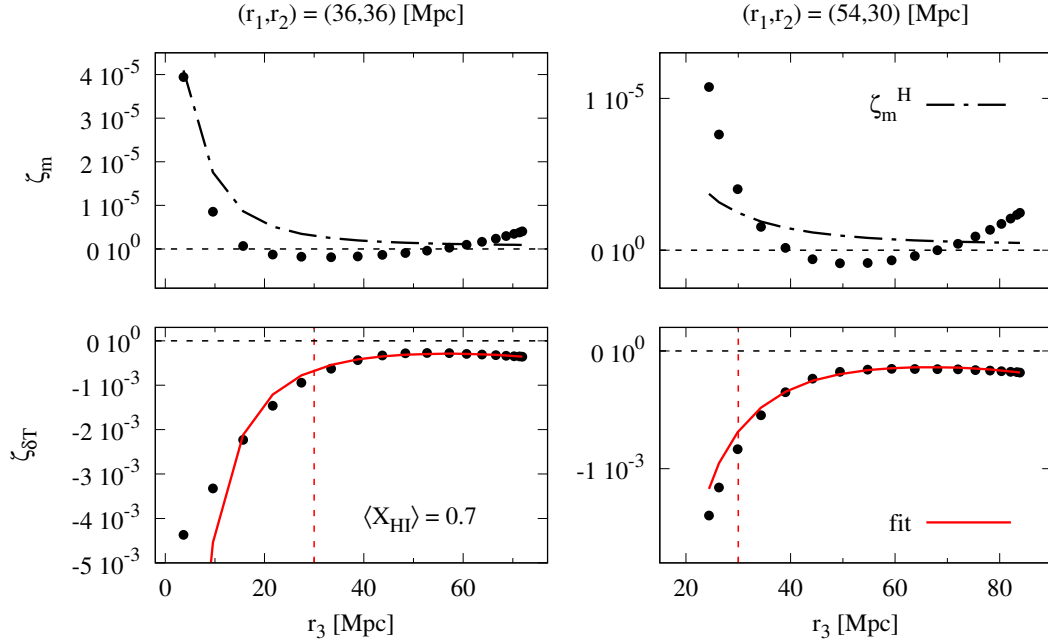


Figure 5. The 21cm 3PCF for two triangles configurations, defined by the fixed legs (r_1, r_2) versus the triangle for different sizes of the third leg r_3 . The smallest and largest r_3 values correspond to collapsed and relaxed triangles with opening angles of 0 and 180 degree respectively. Top panels show measurements of the matter 3PCF (black dots), in comparison to the hierarchical matter 3PCF $\zeta^H \equiv \xi_{12}\xi_{13} + \text{perm}$ (black dashed-dotted lines). The bottom panels show the corresponding 3PCF for δT together with fits to leading order prediction from the bias model in equation (7) (red solid line). The minimum scale used for the fit of 30 Mpc is marked by a vertical red dashed line. Note that the error bar can be smaller than the symbol size.

amplitude becomes positive, while the slope becomes negative at large scales. Again, this behaviour is well described by the fits to equation (7) on scales between 30 and 90 Mpc, while we find strong deviations between fits and measurements at small scales. An interesting small scale feature, is a local minimum at $r_3 \simeq 10$ and 20 Mpc for $\langle x_{\text{HI}} \rangle = 0.99$ and $\langle x_{\text{HI}} \rangle = 0.95$ respectively. This feature may be associated with the a small scale increase of the 21cm bispectrum, predicted by Majumdar et al. (2017) for randomly distributed ionized bubbles. These authors also found a similar feature in the 21cm bispectrum measurements from simulations.

We now aim at testing the quadratic bias model prediction for the 21cm 3PCF on a larger range of scales by jointly fitting larger sets of triangles. In Fig. 7 we show 3PCF measurements from 15 triangle configurations, defined by the fixed legs (r_1, r_2) at the redshifts $z = 13.49$ and 9.77 , with $\langle x_{\text{HI}} \rangle = 0.99$ and 0.7 respectively. The 3PCF is multiplied by the overall triangle scale $(r_1 r_2 r_3)^{1/3}$ to decrease the strong scale dependence of the signal, simplifying a visual comparison the different measurements. Note that this multiplication modifies the overall shape of the 3PCF, which can be seen by comparing results for $r_1 = r_2 = 48$ Mpc to the results from Fig. 6.

We fit the measurements in 6 scale bins (each containing 40 triangles) to verify the large-scale dependence of the 3PCF model fits and the resulting bias parameters. We find $\simeq 2\sigma$ deviations for the largest triangle bin with $\langle (r_1 r_2 r_3)^{1/3} \rangle = 77.4$ Mpc. For the smallest scale bin with $\langle (r_1 r_2 r_3)^{1/3} \rangle = 37.6$ Mpc deviations can be up to 3 (10) σ for $\langle x_{\text{HI}} \rangle = 0.99$ (0.7). These values can correspond to

relative deviations of more than 50% for $(r_1 r_2 r_3)^{1/3} \gtrsim 60$ Mpc and $\langle x_{\text{HI}} \rangle \lesssim 0.6$, while we find $\simeq 20\%$ deviations for $30 \gtrsim (r_1 r_2 r_3)^{1/3} \gtrsim 60$ Mpc and higher global neutral fractions (see Fig. C1). This latter figure also suggests, that the lower significance of deviations at large scales might be attributed to an increase of the measurement errors with scale. However, one could also expect the perturbative approximations, incorporated in bias model, to work better at larger scales. The significance of the deviations reduces in some cases strongly, when ignoring off-diagonal elements in the covariance when computing the χ^2 deviations. This indicates, that these off-diagonal elements have a strong impact on the fits and should not be ignored. It is therefore important to reduce noise in the covariance estimates, which we attempt by using the aforementioned SVD technique and a relatively large number of realizations.

The goodness of the 21cm 3PCF fits in the different triangle scale bins is shown as the minimum χ^2 per degree of freedom (*d.o.f*) in Fig. 8 for various global neutral fractions. The degree of freedoms are the number of modes in the covariance matrix with singular values above the shot-noise limit, from which we compute the χ^2 values. In addition to results based on scales bins with 40 triangles, we also show $\chi^2/\text{d.o.f}$ values for smaller and larger bins with 20 and 60 triangles respectively, verifying the robustness of our fits. We find that for scales above 60 Mpc the $\chi^2/\text{d.o.f}$ values between 1 and 10, independently from the binning. Given our small measurement errors, which result from the large total simulation volume of our 200 realizations, the goodness of fit values indicate a reasonable agreement between model and measurements. The $\chi^2/\text{d.o.f}$ values strongly in-

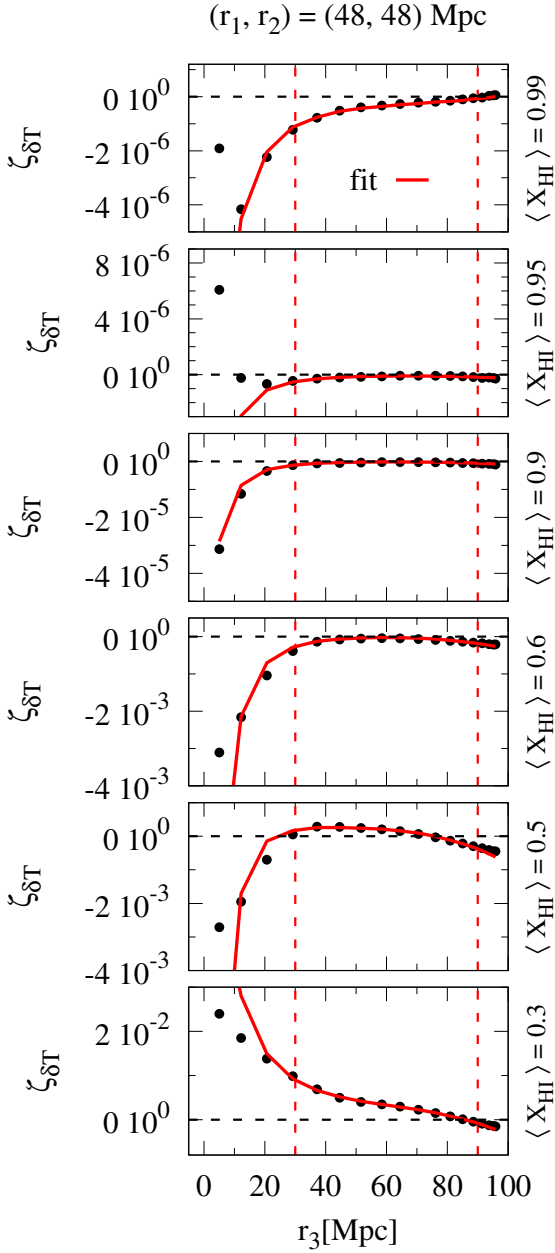


Figure 6. 21cm 3PCF for triangles with $r_1 = r_2 = 48$ Mpc for 18 opening angles between 0 and 180 degree versus the corresponding leg sizes r_3 . Each panel shows results for different neutral fractions $\langle x_{\text{HI}} \rangle$. Black dots show mean measurements from 200 realizations with 1σ error bars. Solid red lines show fits to the leading order prediction from the bias model. The fitting range is marked by vertical red dashed lines.

crease for lower neutral fractions, which is another indication for a break down of the leading order 3PCF bias model. The increase of the $\chi^2/d.o.f$ values at small scales might be attributed to the same effect. However, the smaller measurement errors at small scales also increase the significance between measurements and model fits, which lines up with our conclusions drawn from Fig. 7.

4 BIAS COMPARISON

In the last section we found that the leading order bias expansions of the 21cm 2PCF and 3PCF provide a reasonable fits to the measurements in our simulations at early times and large scales. In this section we focus on this regime, studying the bias parameters obtained from these fits in two ways. We will start by verifying the consistency of the bias parameters, obtained from the 2PCF and the 3PCF fits in Section 4.1. In Section 4.2 we will test if the deterministic quadratic bias model is in agreement with the relation between the fluctuations of δT and matter, which we measure directly in the simulation.

4.1 Bias from correlation functions

Examples of our 3PCF bias constraints are presented as 68.3% and 95.5% confidence regions in the $b_1 - b_2$ parameter space in Fig. 9. These results are obtained from 40 triangle with an average scale of $(r_1 r_2 r_3)^{1/3} \simeq 77.4$ Mpc, which are shown as the largest scale bin in Fig. 7. We find the linear bias b_1 to be positive for $\langle x_{\text{HI}} \rangle = 0.99$ and negative at later times, with values between $-5 \lesssim b_1 \lesssim 1$. The initially positive values of our b_1 measurements originate from the fact that the HI distribution follows the matter density before reionization starts. Later on, the first ionized regions with zero 21cm emission form around the largest matter overdensities (see Fig. 1), leading to an anti-correlation between the 21cm signal and the matter fluctuations, which is described by a negative bias (see also Section 4.2). The quadratic bias b_2 is negative at all considered stages of reionization and has larger absolute amplitudes than b_1 in the range $-5 \lesssim b_2 \lesssim -25$ with a minimum at $\langle x_{\text{HI}} \rangle \simeq 0.7$. We find that the degeneracy between the two parameters is relatively weak, while the uncertainty on b_2 is significantly larger than for b_1 . The latter result might be attributed to the fact that b_1 appears in the ζ_m and ζ_m^H contributions to $\zeta_{\delta T}$ in equation (7) differently and is therefore better constrained than b_2 , which appears only in the ζ_m^H term.

To verify the large scale dependence of our 3PCF bias measurements, we display in Fig. 10 b_1 and b_2 from triangles in different $(r_1 r_2 r_3)^{1/3}$ scale bins versus the mean scale in each scale bin. Results are shown for narrow and broad scale bins, containing 20 and 60 triangles respectively at redshifts with neutral fractions between $\langle x_{\text{HI}} \rangle = 0.99$ and 0.6. Note that we take all triangles into account, while excluding triangles for which one of the legs is smaller than 30 Mpc (as done for the fits, shown in Fig. 5 and 6) affects only results from the smallest scales bin.

We find no significant scale dependence of the bias parameters for redshifts with $\langle x_{\text{HI}} \rangle \gtrsim 0.8$. At lower redshifts with lower neutral fractions we find an increasing scale dependence with $\simeq 10\%$ ($\gtrsim 50\%$) variations of b_1 (b_2), with respect to the average over all scales at $\langle x_{\text{HI}} \rangle = 0.6$. These variations indicate an increasing inaccuracy of the bias model, as reionization progresses, which confirms our 2PCF results. Overall, results from small and large-scale bins are consistent, indicating that they are robust and not strongly affected by uncertainties of the covariance estimation.

The different b_1 measurements in Fig. 10 are compared to the b_1 measurements from the 2PCF fits between 40 and 90 Mpc (see Section 3.2), which is displayed as green solid

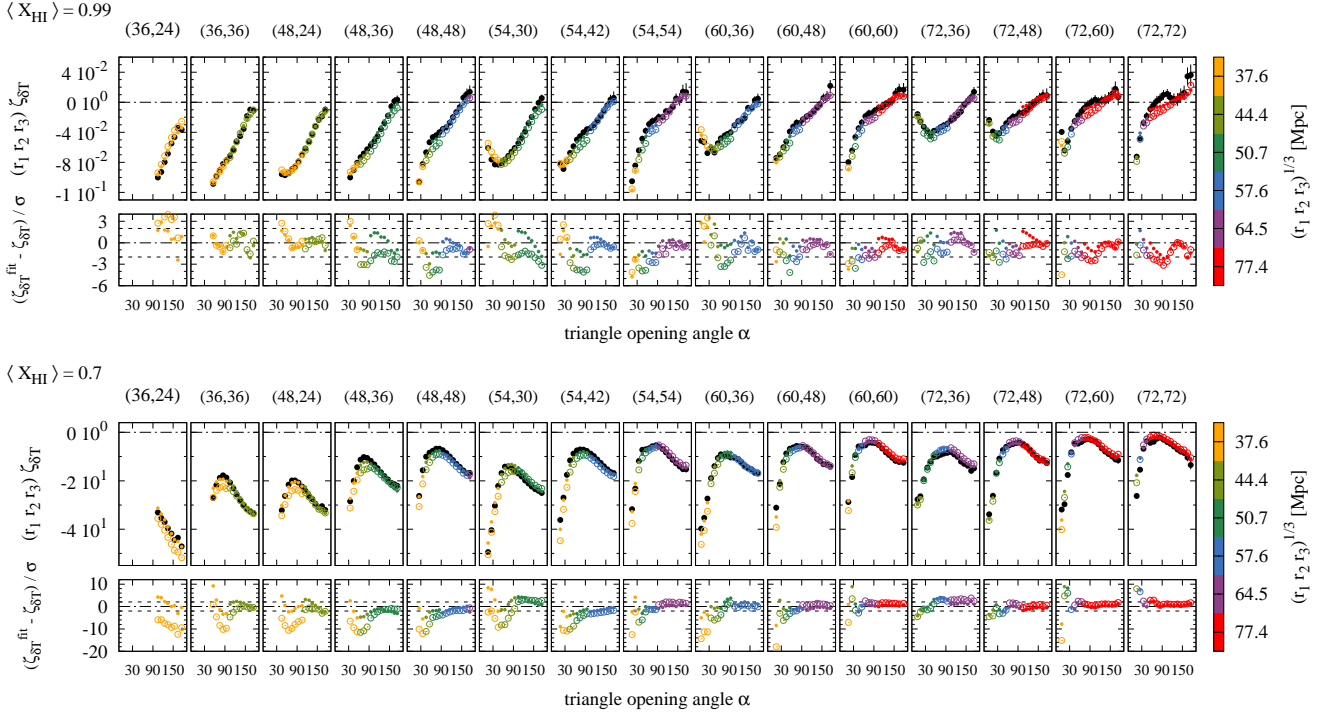


Figure 7. Measurements of the 3PCF the global neutral fractions of $\langle x_{\text{HI}} \rangle = 0.99$ and 0.7 (black dots in the top and bottom panels respectively). Each column shows results from one triangle configuration versus the triangle opening angle. The configurations are defined by the fixed legs (r_1, r_2) as indicated in Mpc on the top. Coloured dots show fits to the leading order bias models prediction. Coloured open circles show fits, without taking into account off-diagonal elements of the error-covariance. The fits are performed separately for triangles in 6 different $(r_1 r_2 r_3)^{1/3}$ scale bins. Each bin contains 40 triangles, which are marked by the same colour. The mean scale of each bin is displayed next to the colour bar on the right. The lower sub-panels show the significance of the deviation between fits and measurements in units of the 1σ measurement errors.

lines. Note that we set the sign of these fits by hand, since the 2PCF only delivers constraints on the absolute value of b_1 (see Section 3.2). We find that the linear bias from the 3PCF is in 10% agreement with 2PCF fits, while deviations are more significant between $\langle x_{\text{HI}} \rangle = 0.9$ and 0.99 , when the linear bias switches its sign from positive to negative. This corresponds roughly to the inaccuracy of the 2PCF fits, shown in Fig. 4.

The dependence of the our bias measurements on the global neutral fraction is displayed in Fig. 11. Results from the 21cm 3PCF are derived from our largest scale bin with 60 triangles, while we also show the 2PCF fits for the linear bias. We find that the dependence of the linear bias from both statistics on $\langle x_{\text{HI}} \rangle$ is well described by a linear relation, while the form of this dependence is less clear for the quadratic bias. We will discuss these results in more detail in paper II of this series.

4.2 Direct measurements of the $\delta_m - \delta_{\delta T}$ bias relation

We now aim at a more direct test of the quadratic bias model, taking advantage of the fact that in the simulation we have access to both, the matter density as well as the 21cm brightness temperature. These quantities, defined in smoothing volumes (i.e. our grid cells) at different positions \mathbf{r} , enables us to directly measure the bias relation $\delta_m - \delta_{\delta T}$ and verify how well it can be described by a determin-

istic function $\delta_{\delta T}(\mathbf{r}) = F[\delta_m(\mathbf{r})]$. Our particular interest is thereby how well this relation agrees with the quadratic bias model from equation (3), when using the bias parameters from the 3PCF measurements.

We show in Fig. 12 a scatter plot of the $\delta_m - \delta_{\delta T}$ relation, for one realization of the simulation as grey dots, while each dot represents δ_m and $\delta_{\delta T}$ measurements from one grid cell. Results are shown for cells with side lengths of 6, 24 and 96 Mpc at redshifts with neutral fractions between 0.99 and 0.6.

The results for 6 Mpc grid cells show that at early times ($\langle x_{\text{HI}} \rangle \gtrsim 0.9$), the 21cm brightness temperature fluctuation $\delta_{\delta T}$ in most cells follows a linear relation to the matter density fluctuations, as expected from equation (1). A departure from this relation occurs for cells with high matter over densities, where the 21cm brightness temperature is lower due to a higher fraction of ionized hydrogen. The effect becomes stronger at lower redshifts, as the reionization proceeds. At lowest redshift with a global neutral fraction of $\langle x_{\text{HI}} \rangle = 0.6$ we find a significant fraction of completely ionized cells with $\delta T = -1$. The trend is apparent for all cell sizes, and provides an understanding of why the linear bias from the correlation function measurements changes its sign from positive to negative with decreasing redshift. The linear bias corresponds to the slope of the $\delta_m - \delta_{\delta T}$ relation at $\delta_m = 0$. The results in Fig. 12 show clearly how this slope follows the trend expected from our previous b_1 measurements, while its value depends on the cell size. For a more detailed compar-

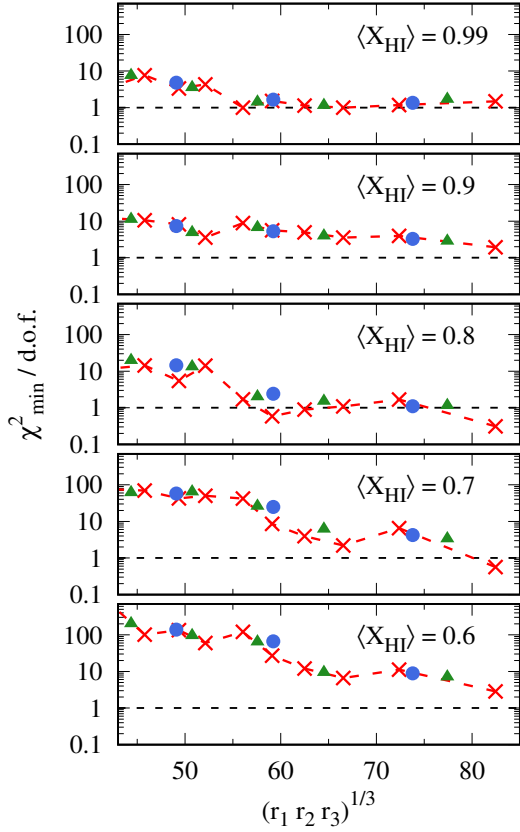


Figure 8. Minimum χ^2 per degree of freedom, quantifying the fitting performance of the quadratic bias model prediction for the 21cm 3PCF from equation (7) for different global neutral fractions $\langle x_{\text{HI}} \rangle$. The model was fitted to 3PCF measurements from triangles in bins, defined by the triangle scale $(r_1 r_2 r_3)^{1/3}$, while the mean scale per bin is shown on the x-axis. Results are shown for 20, 40 and 60 triangles per bin as red, green and blue symbols respectively, while in the first case the symbols are connected with lines to highlight the scale dependence. The degree of freedom is the number of modes in the 3PCF covariance for a particular set of triangles, which is above the noise limit and used for the χ^2 computation.

ison with the quadratic bias model predictions, we show in Fig. 12 the mean $\delta_m - \delta_{\delta T}$ relation in bins of δ_m as black dots. We find this mean to be well approximated by fits to

$$\delta_{\delta T} = \alpha \operatorname{erfc} \left(\frac{\delta_m - \beta}{\gamma} \right) (1 + \delta_m) - 1 \quad (8)$$

at all considered redshifts and scales (red dashed lines in Fig. 12, while α , β and γ are free parameters. In addition to these fits, we show the prediction of the quadratic bias model with 3PCF bias parameters as solid blue lines. The 3PCF bias parameters were measured, using 60 triangles with $\langle (r_1 r_2 r_3)^{1/3} \rangle \simeq 73.8$ Mpc, covering the largest scales in our triangles sample (see Fig. 10). Comparing the quadratic bias model to the mean direct measurements in Fig. 12, we find a good agreement for large grid cells with 96 Mpc side lengths. An exception are the results for $\langle x_{\text{HI}} \rangle = 0.9$ for which the predicted slope of the $\delta_m - \delta_{\delta T}$ is steeper than expected from the direct measurements. This result indicates that the linear bias measurements from the 3PCF is

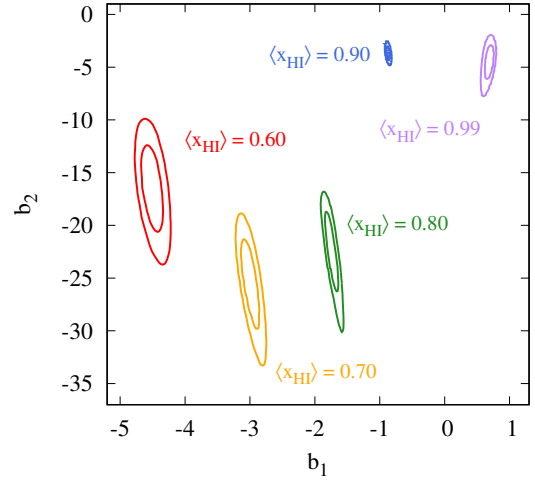


Figure 9. Confidence levels of the linear and quadratic bias parameters from fits of the quadratic bias model prediction for the 21cm 3PCF to measurements in simulations for different neutral fractions $\langle x_{\text{HI}} \rangle$. Contours enclose regions with $\chi^2 - \chi^2_{\min} \lesssim 2.30$ and $\lesssim 6.17$, which corresponds to 68.3 and 95.4% probabilities, assuming a two-dimensional Gaussian distribution. The fits are based on 40 triangles from our sample with the largest $(r_1 r_2 r_3)^{1/3}$ values between 90.68 and 77.4 Mpc. (see Fig. 7).

too low at this stage of reionization. This finding is consistent with our bias comparison from Fig. 10 and can probably attributed to a break down of the 21cm 3PCF bias model, as indicated by the high $\chi^2/\text{d.o.f.}$ values for $\langle x_{\text{HI}} \rangle = 0.9$, shown in Fig. 8. For cells with side 24 Mpc side lengths, the quadratic model is a good approximation $\delta_m \simeq 0$, while clear deviations occur at the tails of the δ_m distribution. For the grid of 6 Mpc cells, on which we measured most of the correlation functions (see Section 3.3), we find that the quadratic bias model differs from the direct measurements for all values of δ_m . This result indicates that the residuals from the mean bias relation may not be random, but spatially correlated. They can hence affect the 3PCF measurements, as well $\delta_{\delta T}$ values at large smoothing scales and modify the measured bias parameters. This effect is subject of ongoing investigations.

5 SUMMARY AND CONCLUSIONS

We studied two- and three-point correlation functions of the 21cm brightness temperature δT (referred to as 21cm 2PCF and 3PCF respectively) during the epoch of reionization. The goal of our study was to characterize the 21cm 2PCF and, for the first time, the 21cm 3PCF in configuration space for different redshifts, scales and triangle shapes, using measurements in simulations. Based on these measurements we tested how well the 21cm 2PCF and 3PCF can be described by the local quadratic bias model, which has been commonly employed for relating the 2PCF and 3PCF of galaxies and halos to the corresponding statistics of the underlying dark matter field.

Our simulations are produced by the semi-numerical code 21cmFAST (Mesinger et al. 2011), with which we generate 200 realizations of the 21cm brightness temperature

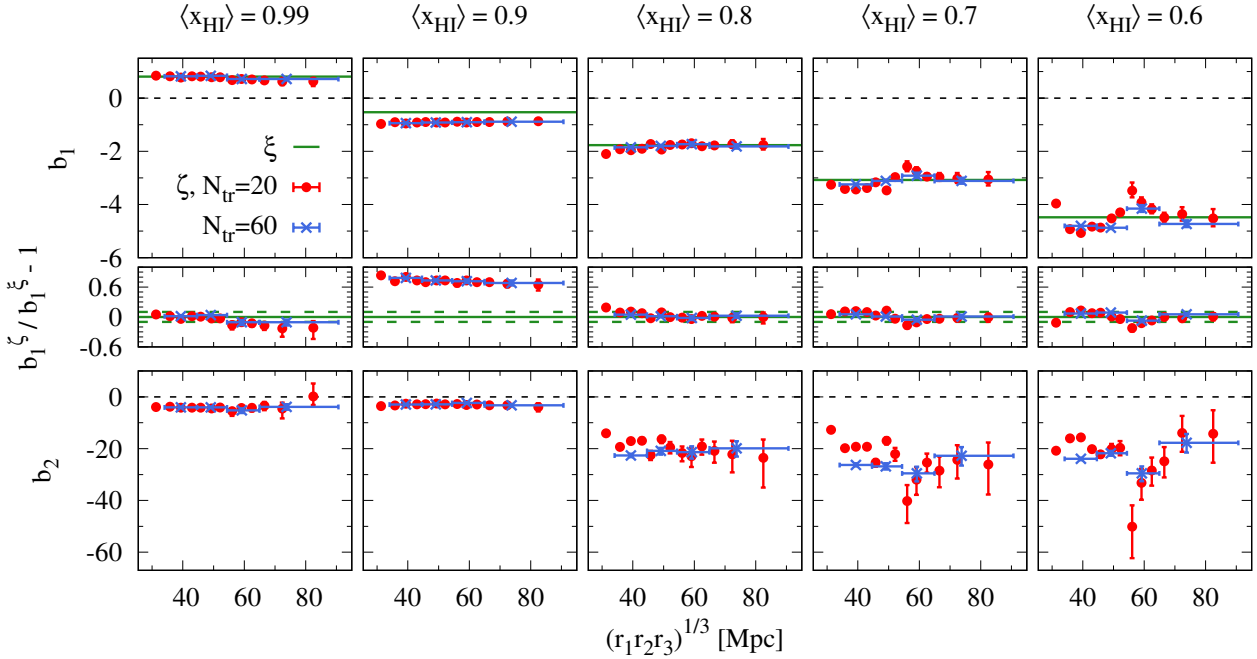


Figure 10. *Top:* Linear bias parameters, measured from fits to the 21cm 3PCF using triangles in bins of the triangles scale $(r_1 r_2 r_3)^{1/3}$, as shown in Fig. 7. Results are shown for scale bins with 20 and 60 triangles as red and blue dots respectively. The linear bias from fits to the 2PCF from Fig. 4 is shown as solid green line with 10% deviations marked by green dashed lines. Each column shows results for different ionized fractions $\langle x_{\text{HI}} \rangle$. *Center:* Relative difference between b_1 from 2PCF and 3PCF fits. *Bottom:* Corresponding measurements of the quadratic bias from the 21cm 3PCF.

and the underlying matter field with different random initial conditions. This set of simulations covers a total volume of $\simeq (4.5 \text{ Gpc})^3$, providing small errors as well as error covariance estimates for our 2PCF and 3PCF measurements, which allow for a detailed comparison with the bias model predictions.

Our 21cm 2PCF measurements present a strong redshift evolution, with an amplitude change of 2 – 3 orders of magnitude for neutral fractions in the range between $0.99 \gtrsim \langle x_{\text{HI}} \rangle \gtrsim 0.3$ ($13.5 \gtrsim z \gtrsim 8.4$). This demonstrates a high sensitivity of the 21cm 2PCF to the state of the reionization. The quadratic expansion of the local bias model in equation (3) predicts the matter and 21cm 2PCF are related to each other by the scale independent linear bias factor b_1 at leading order. We find this prediction to describe the measurements at scales between 30 and 90 Mpc with a $\lesssim 20\%$ accuracy (Fig. 4). This means that the impact of the reionization on the large-scale 2PCF can be well characterized by a single parameters, which limits the constraining power of this statistics for reionization models. Strong deviations from the leading order 2PCF bias model occur at scales of $\lesssim 30$ Mpc, which corresponds roughly to the typical size of ionized regions in our simulation (Fig. 3). This finding indicates that the latter need to be taken into account for a detailed modeling of the 21cm 2PCF at small scales and late times, as it has been discussed in the literature (e.g. Furlanetto et al. 2004).

Our measurements of the 21cm 3PCF show a strong dependence on the triangle opening angles, as well as on the overall triangle size (defined as $(r_1 r_2 r_3)^{1/3}$, e.g. Fig. 7). For a fixed triangle shape, we find a stronger change

of the amplitude than for the 2PCF by up to four orders of magnitude in the considered redshift range (Fig. 6). The strong dependence on the triangle opening angle shows, that the 3PCF does not only probe the scale dependence of the 21cm fluctuations, but also their morphology. It therefore provides access to additional information in the 21cm signal besides its non-Gaussianity, to which the 2PCF is not sensitive. The leading-order approximation of 21cm 3PCF, based on the bias model from equation (7), delivers fits which are in $\sim 2\sigma$ agreement with our measurements (Fig. 7) for triangles with $(r_1 r_2 r_3)^{1/3} \gtrsim 60$ Mpc (given our small measurements errors). A notable small scale feature of our 3PCF measurements, which is not described by the bias model, is the increase of the amplitude at the smallest scales at early times ($\langle x_{\text{HI}} \rangle \gtrsim 0.9$, Fig. 6). Such an increase has also been reported by Majumdar et al. (2017) for bispectrum measurements in simulations, as well model predictions, based on randomly distributed ionized bubbles.

The dependence of our best fit bias parameters on the chosen triangle scale range, shown in Fig. 10, is within the expected $1 - 2\sigma$ uncertainty for $\langle x_{\text{HI}} \rangle \gtrsim 0.7$. At $\langle x_{\text{HI}} \rangle = 0.6$ this scale dependence becomes more significant, indicating a breakdown of the leading order 3PCF bias model, which we already noticed in the 2PCF analysis (Fig. 4). The linear bias from the 3PCF is compared to the results from the 2PCF in the top panel of Fig. 10. The comparison reveals a $\simeq 10\%$ agreement in the considered redshift range (with $\langle x_{\text{HI}} \rangle > 0.6$), when the analysis is restricted to large triangles with $(r_1 r_2 r_3)^{1/3} \gtrsim 60$ Mpc. The results is consistent with the aforementioned inaccuracy of the linear bias model for the 2PCF at large scales. An exception are the strong relative

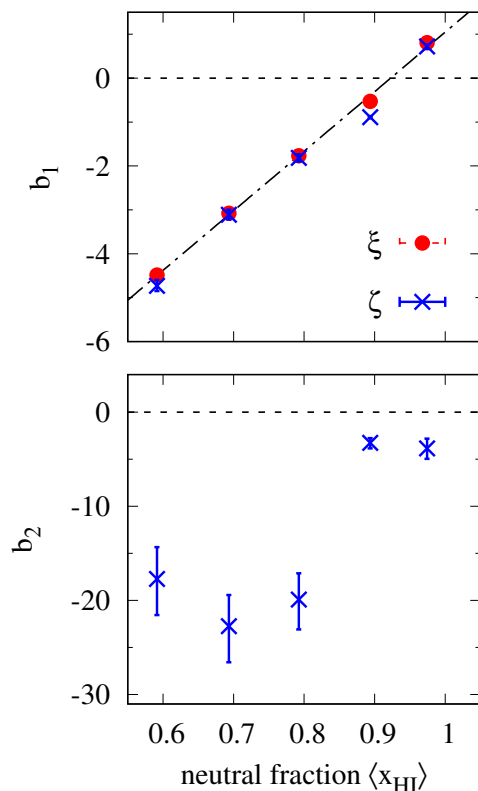


Figure 11. Linear and quadratic bias parameters (top and bottom panels respectively) versus the global neutral fraction $\langle x_{\text{HI}} \rangle$. Red and blue symbols show measurements derived from the 21cm 2PCF and 3PCF respectively. The latter are derived from the 60 largest triangles in our analysis, with the average scale of $\langle (r_1 r_2 r_3)^{1/3} \rangle = ()$ Mpc. The evolution of the linear bias with neutral fraction is well fitted by a relation: $b_1 = 13.57 \langle x_{\text{HI}} \rangle - 12.52$, shown as dashed-dotted line.

deviations between the 2PCF and 3PCF b_1 measurements at $\langle x_{\text{HI}} \rangle = 0.9$, where the b_1 amplitude is close to zero. One possible reason for this effect might be a low signal to noise ratio in the measurements, which could affect the fits. However, further investigation will be needed to understand this finding.

Up to this point we tested the quadratic bias model for the assumed deterministic $\delta_{\delta T} = F(\delta_m)$ relation via its leading order prediction for the 2PCF and 3PCF. In the final step of our analysis, we conducted a more direct test of the model, by comparing its predicted $\delta_m - \delta_{\delta T}$ relation, to direct measurements in the simulations (Fig. 12). For this comparison we employ the linear and quadratic bias parameters, measured from the 3PCF at large scales. We find strong deviations between the bias model prediction and the direct average value of $\delta_{\delta T}$ in bins of δ_m when using small smoothing scales of 6 Mpc for the direct measurements. However, for large smoothing scales of 96 Mpc, we find an overall good agreement in the considered redshift range. Another interesting finding is that the average $\delta_m - \delta_{\delta T}$ relation is well approximated by the analytic expression, given by equation (8). The physical interpretation of this expression is the subject of our followup work.

Overall our results show that the quadratic bias

provides a consistent description of the 21cm 2PCF and 3PCF on scales larger than $\simeq 30$ Mpc at early times of the reionization with $\langle x_{\text{HI}} \rangle \gtrsim 0.7$. It further describes the $\delta_m - \delta_{\delta T}$ well at large smoothing scales of $\gtrsim 30$ Mpc. The latter result suggests that the linear and bias parameter measurements from the 21cm 3PCF can provide insights to the process leading to the reionization from upcoming 21cm observations.

Inferring the bias parameters from the observed 21cm 3PCF in three dimensions further requires an understanding of how the 21cm 3PCF is affected by redshift space distortions. Alternatively, one could also study only its transverse component via the projected 21cm 3PCF in redshift bins. In this latter case, we expect that the quadratic bias model also describes the 21cm 3PCF as well, as shown by (Zheng 2004). The consistency between linear bias measurements from the 2PCF and the 3PCF opens up the possibility to use the 21cm 3PCF to break the degeneracy between the linear growth factor and the linear bias parameter, which appears in the transverse component of the 2PCF. A joint analysis of the projected 21cm 2PCF and 3PCF in future 21cm surveys could therefore provide growth measurements and hence constraints on cosmological models at unprecedented redshifts. In that sense the 3PCF would also allow to disentangle the astrophysical effects on the 21cm two-point statistics from those of the underlying cosmology. However, our analysis also revealed clear short-comings of the quadratic bias model description, in particular at small scales and late times of reionization. An improvement of the model might require further investigation of the residuals from the average $\delta_{\delta T} - \delta_m$ bias relation as well as an expansion of the 21cm 2PCF and 3PCF beyond leading order.

ACKNOWLEDGMENTS

K. H. is supported by the International Postdoctoral Fellowship from the Ministry of Education and the State Administration of Foreign Experts Affairs of China. Y.M. is supported in part by the National Natural Science Foundation of China (Grant No. 11673014, 11543006), by the Chinese National Youth Thousand Talents Program, and by the Opening Project of Key Laboratory of Computational Astrophysics, National Astronomical Observatories, Chinese Academy of Sciences.

References

- Baldauf T., Seljak U., Desjacques V., McDonald P., 2012, *Phys. Rev. D*, **86**, 083540
- Barriga J., Gaztañaga E., 2002, *MNRAS*, **333**, 443
- Bernardeau F., Colombi S., Gaztañaga E., Scoccimarro R., 2002, *Phys. Rept.*, **367**, 1
- Bharadwaj S., Pandey S. K., 2005, *MNRAS*, **358**, 968
- Chan K. C., Scoccimarro R., Sheth R. K., 2012, *Phys. Rev. D*, **85**, 083509
- Field G. B., 1958, *Proceedings of the IRE*, **46**, 240
- Fry J. N., Gaztanaga E., 1993, *ApJ*, **413**, 447
- Furlanetto S. R., 2006, *MNRAS*, **371**, 867
- Furlanetto S. R., Zaldarriaga M., Hernquist L., 2004, *ApJ*, **613**, 1
- Furlanetto S. R., Oh S. P., Briggs F. H., 2006, *Phys. Rept.*, **433**, 181
- Gaztañaga E., Scoccimarro R., 2005, *MNRAS*, **361**, 824

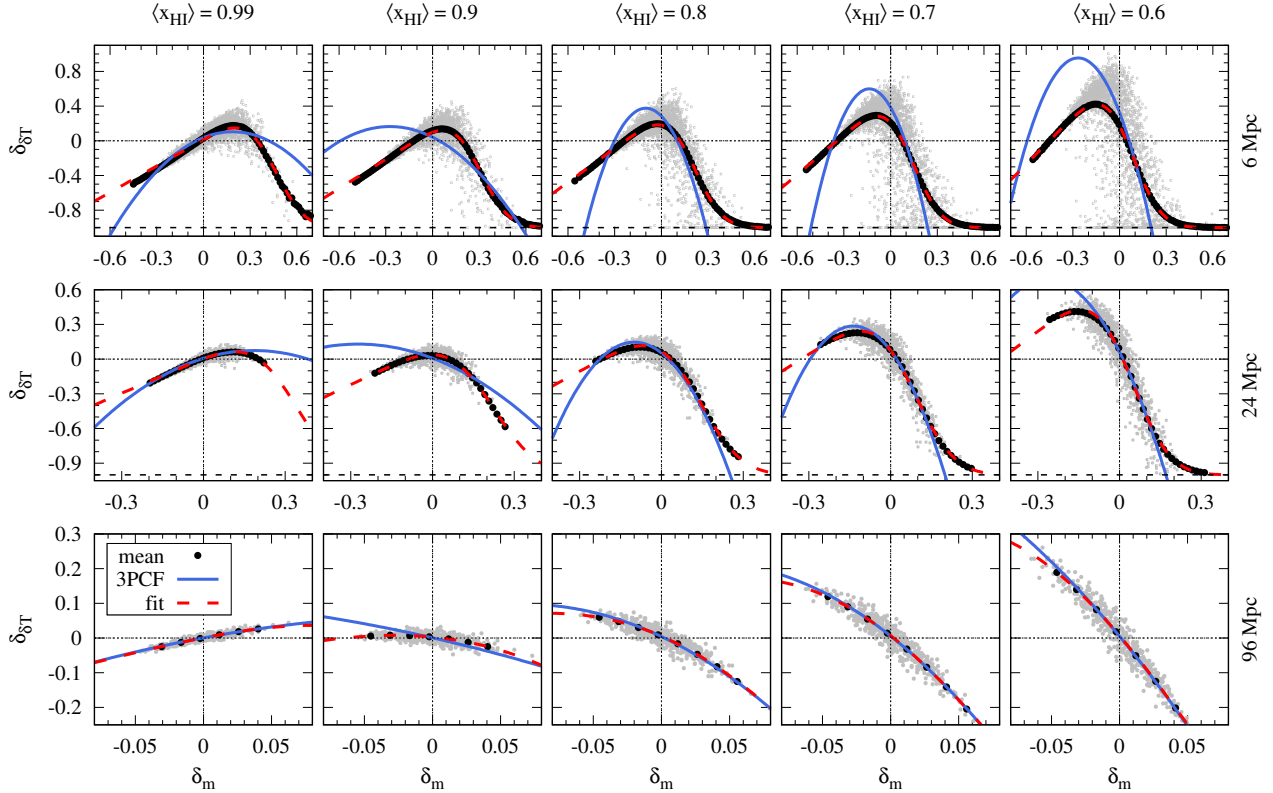


Figure 12. Fluctuations in the 21 brightness temperature δT versus those of the matter density. Grey dots show direct measurements from one realization, while each dot represents a measurement in one grid cell. Black dots show the mean δT fluctuations in bins of δ_m , averaged over our 200 realizations. Red dashed lines show fits to equation (8). Blue solid lines show the quadratic bias model from equation (3) with the bias parameter measured from the 3PCF, derived from the 60 largest triangles in our analysis, with $\langle (r_1 r_2 r_3)^{1/3} \rangle \simeq 73.8$ Mpc, shown in Fig. 10. Columns show results for different neutral fractions $\langle x_{\text{HI}} \rangle$. The top, central and bottom rows show results for grid cells with side lengths of 6, 24 and 96 respectively. Direct measurements are diluted for each cell size differently. Note that the quadratic bias model is the same for different cell sizes, but differs for different $\langle x_{\text{HI}} \rangle$.

Hartlap J., Simon P., Schneider P., 2007, *A&A*, **464**, 399
Hoffmann K., Gaztanaga E., Scoccimarro R., Crocce M., 2017, preprint, ([arXiv:1708.08941](https://arxiv.org/abs/1708.08941))
Lidz A., Zahn O., McQuinn M., Zaldarriaga M., Dutta S., Hernquist L., 2007, *ApJ*, **659**, 865
Liu A., Parsons A. R., 2016, *MNRAS*, **457**, 1864
Majumdar S., Pritchard J. R., Mondal R., Watkinson C. A., Bharadwaj J., Mellema G., 2017, preprint, ([arXiv:1708.08458](https://arxiv.org/abs/1708.08458))
McQuinn M., Zahn O., Zaldarriaga M., Hernquist L., Furlanetto S. R., 2006, *ApJ*, **653**, 815
Mesinger A., Furlanetto S., 2007, *ApJ*, **669**, 663
Mesinger A., Furlanetto S., Cen R., 2011, *MNRAS*, **411**, 955
Pober J. C., et al., 2014, *ApJ*, **782**, 66
Pritchard J. R., Furlanetto S. R., 2007, *MNRAS*, **376**, 1680
Pritchard J. R., Loeb A., 2012, *Reports on Progress in Physics*, **75**, 086901
Raste J., Sethi S., 2017, preprint, ([arXiv:1711.03827](https://arxiv.org/abs/1711.03827))
Schmit C. J., Pritchard J. R., 2017, preprint, ([arXiv:1708.00011](https://arxiv.org/abs/1708.00011))
Shimabukuro H., Yoshiura S., Takahashi K., Yokoyama S., Ichiki K., 2016, *MNRAS*, **458**, 3003
Shimabukuro H., Yoshiura S., Takahashi K., Yokoyama S., Ichiki K., 2017, *MNRAS*, **468**, 1542
Sokasian A., Yoshida N., Abel T., Hernquist L., Springel V., 2004, *MNRAS*, **350**, 47
Zaldarriaga M., Furlanetto S. R., Hernquist L., 2004, *ApJ*, **608**, 622

Zheng Z., 2004, *ApJ*, **614**, 527

APPENDIX A: EFFECT OF SIMULATION BOX SIZE ON 21CM 2PCF MEASUREMENTS

The size of the simulation box determines the wavelength of the largest mode, in the matter density field of our simulation. The box size can therefore affect matter and 21cm correlation functions, which we measure in the simulations on large scales.

We test how strongly our 21cm 2PCF measurements are affected by the chosen box size by generating 14 realizations, which have twice the side length (i.e. $L_{\text{box}} = 1536$ Mpc) than the 200 realizations, used in our analysis. In the top panel of Fig. A1 we compare the 21cm 2PCF measurements for both sizes at the redshift $z = 9.77$ ($\langle x_{\text{HI}} \rangle = 0.7$). Our results show that the box size affects the measurements on large scales. The bottom shows the square root of the ratio of the 21cm and matter 2PCF, with the linear bias fit to the measurements from our 200 realizations. This results show that the effect of the box size become significant on scales of $\gtrsim 90$ Mpc.

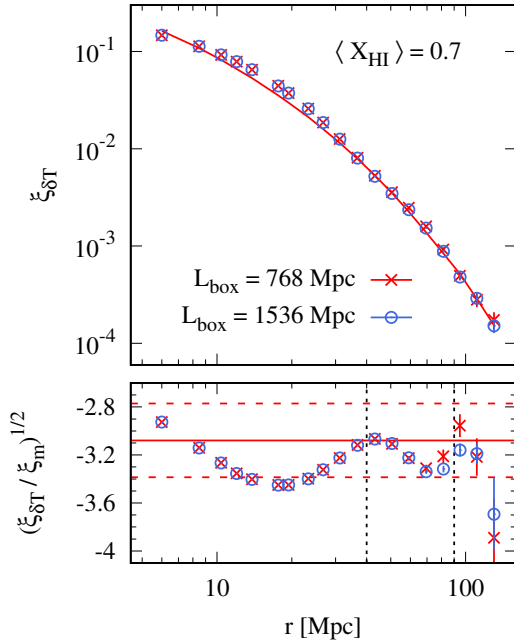


Figure A1. *Top:* mean 21cm 2PCF, measured from 200 (14) realizations with boxes of side length $L_{\text{box}} = 768$ (1536) Mpc for global neutral fraction of $\langle x_{\text{HI}} \rangle = 0.7$. *Bottom:* square root for the ratio of the 21cm and matter 2PCF. The black solid line shows a fit to the linear bias model, with 10% deviations marked as dashed lines. Vertical dotted lines mark the scale range, on which the measurements are fitted.

APPENDIX B: COVARIANCES AND χ^2 FITTING

We fit the bias model predictions for the 21cm 2PCF and 3PCF (equation (5) and (7) respectively) to the corresponding measurements by a χ^2 minimization. We therefore explore the parameter space, searching for the minimum of

$$\chi^2 = \sum_{ij}^N \Delta_i \hat{C}_{ij}^{-1} \Delta_j, \quad (\text{B1})$$

where $\Delta_i \equiv (X_i^{\text{model}} - \langle X \rangle_i) / \sigma_i$. The mean measurements for a certain scale or triangle i over the N_{sim} realizations are denoted as $\langle X \rangle_i$, while X_i^{model} are the corresponding predictions. The variance of $\langle X \rangle_i$ is given by $\sigma_i^2 = \langle (X_i - \langle X \rangle_i)^2 \rangle / N_{\text{sim}}$. The factor $1/N_{\text{sim}}$ accounts for the fact that we are interested in the errors on the mean measurements, rather than those on measurements from individual realizations. The normalized covariance matrix is hence given by

$$\hat{C}_{ij} = \langle \Delta_i \Delta_j \rangle / N_{\text{sim}}, \quad (\text{B2})$$

with $\Delta_i \equiv (X_i - \langle X \rangle_i) / \sigma_i$. We show examples of our \hat{C}_{ij} measurements for the 2PCF and 3PCF in Fig. B1 and B2 respectively. In both cases the covariance matrix has strong off-diagonal elements, in particular at small scales. This indicates that knowledge of the covariance is essential for constraining theory models 21cm 2PCF and 3PCF measurements in future observations. Based on these covariance measurements, our fits are performed for measurements

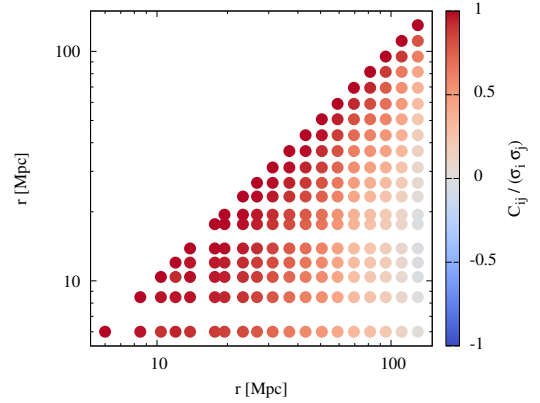


Figure B1. Normalized covariance of the 21cm 2PCF at $\langle x_{\text{HI}} \rangle = 0.7$, estimated from measurements in 200 realizations of our simulation for different scales r .

from $N < N_{\text{sim}}$ different scales or triangles, to ensure that the covariance is invertible (Hartlap et al. 2007).

We find that 3PCF fits based on equation (B1) can be very sensitive to small changes in the selected triangle sample, which may be caused by noise in our covariance estimation from the only 200 realizations. To reduce this noise, we follow Gaztañaga & Scoccimarro (2005) by performing a Singular Value Decomposition of the covariance (hereafter referred to as SVD), i.e.

$$\hat{C}_{ij} = (U_{ik})^\dagger D_{kl} V_{lj}. \quad (\text{B3})$$

The diagonal matrix $D_{kl} = \delta_{kl} \lambda_k^2$ consists of the singular values λ_j (SVs), while the corresponding normalised modes $\hat{\mathbf{M}}_i$ form the matrix U . The modes associated to the largest SVs may be understood analogously to eigenvectors. The χ^2 expression from equation (B1) can now be approximated by writing it in terms of the most dominant modes

$$\chi^2 \simeq \sum_i^{N_{\text{mode}}} \langle \Delta_i \hat{\mathbf{M}}_i \rangle^2 / \lambda_i^2. \quad (\text{B4})$$

Note that here $\langle \dots \rangle$ denotes the scalar product, i.e. the projection of Δ_i on $\hat{\mathbf{M}}_i$, while Δ_i is the same quantity which appears in equation (B1).

Fig. B3 shows that \hat{C}_{ij} is typically dominated only by a few modes. Assuming that the modes with the lowest SVs can be associated with measurement noise, we use only SVs with values larger than the sampling error estimate (i.e. $\lambda^2 \gtrsim \sqrt{2/N_{\text{sim}}}$) for our χ^2 computation, as suggested by Gaztañaga & Scoccimarro (2005). The number of selected modes is hence the degree of freedom in our χ^2 estimation, i.e. d.o.f. = $N_{\text{mode}} < N_{\text{bin}} < N_{\text{sim}}$. Note that the description above matches in various parts Section 2.4 in Hoffmann et al. (2017), who do a very similar analysis for the 3PCF of haloes.

APPENDIX C: RELATIVE DEVIATIONS OF 21CM 3PCF FITS FROM MEASUREMENTS

This paper has been typeset from a $\text{\TeX}/\text{\LaTeX}$ file prepared by the author.

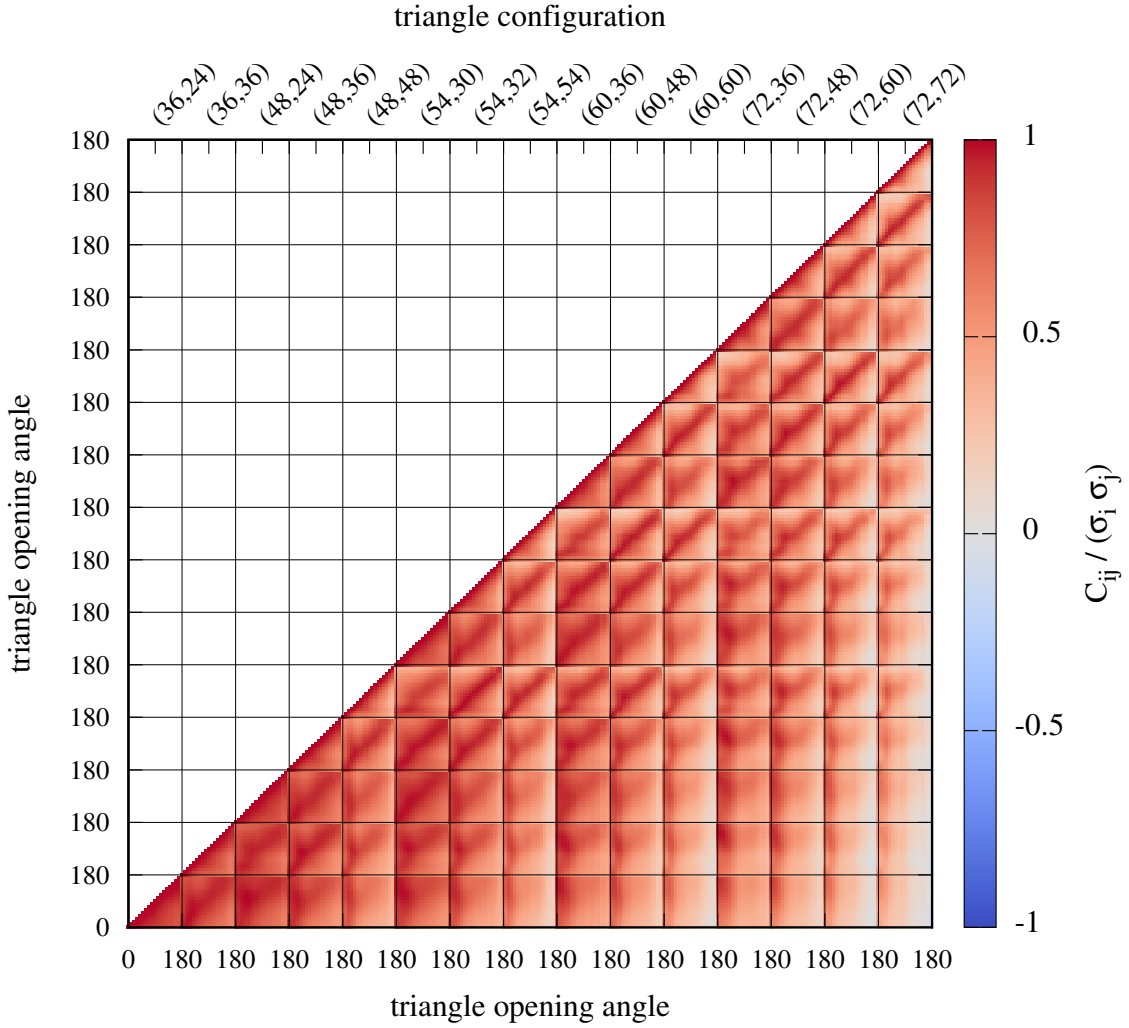


Figure B2. Normalized covariance of the 21cm 3PCF at $\langle x_{\text{HI}} \rangle = 0.7$, estimated from measurements in 200 realizations of our simulation. Each tile shows results from different triangle configurations, defined by the fixed triangle legs (r_1, r_2). The leg sizes are shown in Mpc at the top of each column. The 3PCF was measured for each configuration at 18 opening angles between 0 and 100 degree, leading to a total of 270 triangles from all configurations.

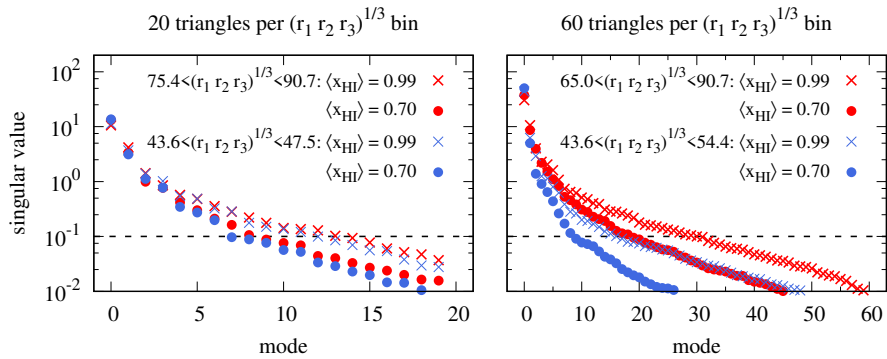


Figure B3. Singular values of different modes for examples of covariance matrices used in this work. The black dashed line marks the shot noise limit of $\sqrt{2/N_{\text{sim}}}$, below which modes are neglected in the χ^2 calculation.

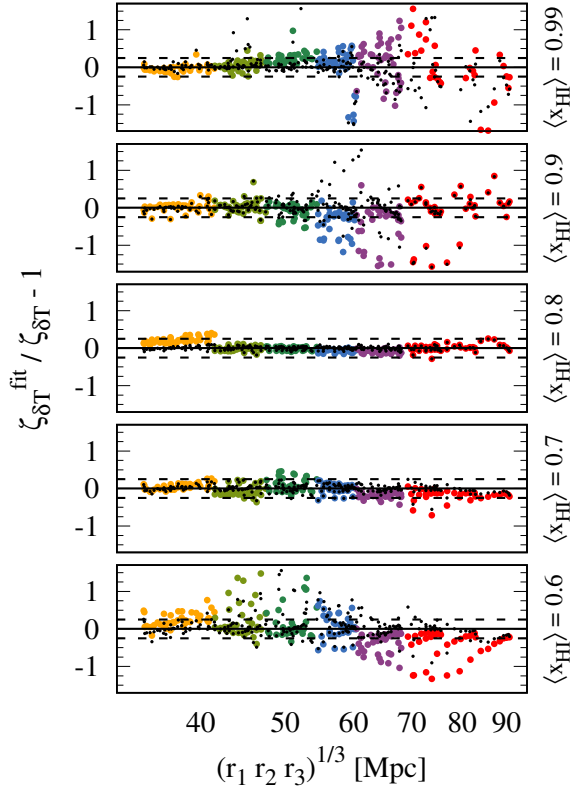


Figure C1. Relative deviations between the measurements of the 21cm 3PCF and fits to the latter based on the quadratic bias model, versus the triangle scale. The panels show results for various redshifts with different global neutral fractions. The fits are performed separately for triangles in 6 different scale bins. Each bin contains 40 triangles, which are marked by the same colour. Black dots show results for fits, which do not take off-diagonal elements of the error-covariance into account. Relative deviations of $\pm 25\%$ are marked by dashed lines.